

Predicting maximum force in SPIF for different materials

Rafael Gustavo Schreiber (✉ rafael.schreiber@ifsc.edu.br)

Federal Institute of Education Science and Technology of Santa Catarina: Instituto Federal de Educacao Ciencia e Tecnologia de Santa Catarina
<https://orcid.org/0000-0002-6443-7469>

Lucas Santos Savi Mondo

Federal Institute of Education Science and Technology of Santa Catarina: Instituto Federal de Educacao Ciencia e Tecnologia de Santa Catarina

Anderson Daleffe

SATC: Associacao Beneficente da Industria Carbonifera de Santa Catarina

Lirio Schaeffer

Federal University of Rio Grande do Sul: Universidade Federal do Rio Grande do Sul

Research Article

Keywords: SPIF, Maximum Axial Force, FEM, Multiple Regression

Posted Date: April 12th, 2022

DOI: <https://doi.org/10.21203/rs.3.rs-1525758/v1>

License:  This work is licensed under a Creative Commons Attribution 4.0 International License. [Read Full License](#)

Abstract

Knowing the importance of predicting acting forces during the formation process, our research has conducted 27 SPIF experiments in hyperboloid format, followed by Finite Element Method (FEM) simulations to validate the measurements found in order to determine regression equations to estimate maximum axial force in the SPIF process according to material type, sheet initial thickness and tool radius. With that data, we created a general multiple regression model and three other independent models (one for each material). After the experiments, we were able to identify that the maximum axial force increases according to increase in tool radius, plate initial thickness and yield constant values, as well as according to the decrease in strain-hardening exponent. The FEM simulations are in accordance with the experimental values found, and the general regression model has proven to be efficient to describe results, with a maximum percentage error of 11.5% in the regression equation. In the independent regression models, precision was increased and the maximum percentage error in the equations was of 10.9%.

1 Introduction

In Incremental Sheet Forming (ISF), the final shape of the piece being manufactured is defined by the hemispheric-tipped tool's trajectory, which progressively deforms a plane sheet [1]. This is a flexible process that does not require dedicated tools [2] and can be used in the fabrication of individual parts or small lots of parts [3].

Compared to conventional sheet formation processes, in ISF the necessary conformation force is reduced due to localized and successive deformations that occur during the process [4]. Nevertheless, it is fundamental to be able to predict the acting forces during the process in order to select the equipment that will be used, such as a CNC milling machine [5, 6], a CNC lathe [7, 8], a robotic arm [9, 10], or a machine designed for this purpose [11, 12].

The process parameters influence the ISF acting forces, and as such, with an increase in tool radius [13], initial sheet thickness [14], or step-down [15], there is also an increase in the force required to achieve the deformation. Materials with greater yield strength [14, 15] also require greater force for the deformation to occur. However, as tool rotation increases [16], and with it the process temperature [17], there is a decrease in the required force. The feed rate on the other hand presents little influence over the forces applied to the ISF process [18].

Duflou et al. [19] have verified that compared to the tool radius, the sheet's thickness and the wall angle, the step-down is the least relevant factor among the acting forces in the ISF process.

In the ISF process, the axial force component is the one that presents the greater intensity when compared to radial and tangential components [20, 21]. Depending on the shape of the piece that is being conformed by the ISF, the force versus time graph presents different characteristics [22]. However, in the most common shapes (truncated cone and hyperboloid), it is possible to observe that the axial force component shows a peak during the tool's axial movement against the sheet, followed by a lower level during the tool's circular interloping [14, 23].

Li et al. [24] have developed an analytical model based on the superior limit approach to predict tangential forces in SPIF, applying truncated cone conformation with different wall angles and step-downs. This model showed greater accuracy for step-down values lower than 0.5 mm.

Duflou et al. [23] and Aereus et al. [14] have developed regression equations to estimate mean axial force, radial force and tangential force for the truncated cone shape, according to different process parameters and different materials.

Bansal et al. [25] and Chang et al. [4] have also developed analytical models to predict ISF force based on stress and contact area between the piece and the tool. Their models presented greater accuracy when compared to the ones proposed by Aereus et al. [14].

Despite there being several models that allow an estimation of ISF's mean forces, there is still the need to estimate maximum force, which has a fundamental role in the selection of appropriate equipment to perform the conformation. Therefore, our work aims to evaluate the influence of material properties, sheet thickness and tool diameter in the axial force applied to the conformation tool using the Single Point Incremental Forming (SPIF) process.

2 Materials And Methods

In this study, 27 SPIF experiments were conducted testing the fabrication of hyperboloids with different materials, sheet thicknesses and tool radii in order to evaluate what influence these parameters exert on the maximum axial force $F_{z_{max}}$. To validate the force results found in the experiments, three FEM simulations were made. In addition, multiple regressions were also conducted to introduce a prediction method for maximum axial force for each process condition. In Table 1, we have indicated the symbology and the measuring units of the parameters used during the course of this work.

Table 1
Parameters

Symbol	Parameter	Unit
C	Yield Constant	MPa
Fz	Axial force	N
Fz _{max}	Maximum axial force	N
h	Maximum deep	mm
n	Strain-hardening Exponent	-
PE	Percentage error	%
PE _{max}	Maximum percentage error	%
R _t	Tool radius	mm
s	Final thickness	mm
s ₀	Initial thickness	mm
θ	Final wall angle	rad
θ ₀	Initial wall angle	rad

For the experiments, the materials used were AA1200-H14 aluminum, SAE1008 steel and C268 brass sheets, with mechanical thicknesses and properties as indicated in Table 2. The mechanical properties of the materials presented in Table 2 were based on studies by Schreiber et al. [26] for AA1200-H14, Haag and Ferranti [27] for SAE1008 and Maximiliano et al. [28] for C268.

Table 2
Material Properties

Material	Initial thickness, s ₀ (mm)	Yield Strength (MPa)	Tensile Strength (MPa)	Elongation (%)	Modulus of Elasticity (GPa)	Yield Constant, C (MPa)	Strain-hardening Exponent, n (-)
AA1200-H14	0.50 / 0.80 / 1.20	97	117	3.6	70	181.45	0.1080
SAE1008	0.60 / 0.75 / 0.90	265	359	41.5	190	619.86	0.2163
C268	0.50 / 0.81 / 1.06	296	413	37.5	105	734.28	0.2624

2.1 SPIF Experiments with Force Measurement

For this research, the pieces were conformed in a hyperboloid shape (Fig. 1a) using the SPIF process. The hyperboloid shape allows variation in the piece's wall angle (between θ₀ and θ) and thickness (between s₀ and s) according to h depth. All experiments were conducted until the piece reached maximum wall angle and presented a crack. Figure 1b shows a hyperboloid conformation in the final experiment, indicating the location of the crack and the support parts used to fixate the sheet, constituted of a rig, backing plate and blank-holder.

Unidirectional strain gauges, brand Excel and model PA-06-060BA-350L were installed in the conformation tool to measure the axial force during the process, since this is the most intense force in the SPIF process [14]. Figure 2 presents how the link between the strain gauges (Wheatstone bridge circuit), in which four strain gauges (R₁ a R₄), are presented and where bridge exciting voltage is indicated with a V_s, and bridge exit voltage with a V₀. Data acquisition was made using a microcontroller board Arduino MEGA 2560 R3 connected to a computer.

Experiments were made in a Nardini LOGIC 195VS CNC lathe. Figure 3a presents the configuration used for the CNC lathe experiments, indicating the tool, the sheet (fixated on a support system), as well as a turret, chuck and the z axis force measuring system, constituted of strain gauges and microcontroller board.

Figure 3b indicates the tool trajectory and of the part in the CNC lathe, considering that the tool's linear trajectories were conducted by the turret (with a feed rate of 100 mm/min), and the circular trajectories were made by the sheet fixed on the chuck (with a rotation speed of 2 rpm). The step-down used in the experiments was of 1 mm and lubrication was added with a thin layer of VG100 oil. The tool used in this study were fabricated in SAE 1045 steel, quenched and tempered, with radii of 3, 5 and 7.5 mm.

A general equation was determined to estimate the maximum axial force in a SPIF process using multiple regressions according to material property (yield constant C and strain-hardening exponent n), initial sheet thickness and tool radius.

We were also able to determine maximum axial force equations for each material used, in order to verify the sheet's initial thickness and tool radius' influence. Statistical analyses of this work were made using the RStudio software.

To validate the regression models obtained in this work, we used Eq. 1, where PE is the percentage error, X is the data obtained by the regression model and X_{exp} is the data obtained in the experiments.

$$PE = \frac{|X - X_{exp}|}{X_{exp}} \cdot 100 \quad (1)$$

2.2 FEM Simulation

Aiming to validate the axial force data obtained in the experiments using strain gauges, three simulations were made using the Finite Elements Method (FEM) with the Simufact Forming software. The results obtained in the simulations were compared to the experimental data, and the maximum axial force percentage error was calculated for each simulation using Eq. 1. The experiments selected for comparison with the simulation were numbers 7, 14 and 25 (Table 3), in order to compare axial force values in different materials and validate the measurements.

Table 3
SPIF conformability experimental results

Exp.	Material	C (MPa)	n (-)	R_t (mm)	s_0 (mm)	$F_{z_{max}}$ (N)
1	AA1200-H14	181.45	0.1080	3.0	0.50	323.4
2	AA1200-H14	181.45	0.1080	3.0	0.80	515.0
3	AA1200-H14	181.45	0.1080	3.0	1.20	939.6
4	AA1200-H14	181.45	0.1080	5.0	0.50	471.5
5	AA1200-H14	181.45	0.1080	5.0	0.80	745.1
6	AA1200-H14	181.45	0.1080	5.0	1.20	1205.3
7	AA1200-H14	181.45	0.1080	7.5	0.50	638.9
8	AA1200-H14	181.45	0.1080	7.5	0.80	918.6
9	AA1200-H14	181.45	0.1080	7.5	1.20	1595.0
10	SAE1008	619.86	0.2163	3.0	0.60	1485.9
11	SAE1008	619.86	0.2163	3.0	0.75	2157.0
12	SAE1008	619.86	0.2163	3.0	0.90	2508.8
13	SAE1008	619.86	0.2163	5.0	0.60	2000.7
14	SAE1008	619.86	0.2163	5.0	0.75	2668.5
15	SAE1008	619.86	0.2163	5.0	0.90	3203.7
16	SAE1008	619.86	0.2163	7.5	0.60	2947.9
17	SAE1008	619.86	0.2163	7.5	0.75	3567.3
18	SAE1008	619.86	0.2163	7.5	0.90	4508.8
19	C268	734.28	0.2618	3.0	0.50	1071.1
20	C268	734.28	0.2618	3.0	0.81	2067.6
21	C268	734.28	0.2618	3.0	1.06	3378.4
22	C268	734.28	0.2618	5.0	0.50	1450.2
23	C268	734.28	0.2618	5.0	0.81	2619.8
24	C268	734.28	0.2618	5.0	1.06	3566.6
25	C268	734.28	0.2618	7.5	0.50	2110.8
26	C268	734.28	0.2618	7.5	0.81	3672.7
27	C268	734.28	0.2618	7.5	1.06	5413.8

Simulations were made with a 3D simulation type and with solid-shell type elements, available within the Sheet Metal Forming module in the software. The mesh created for each sheet was configured with edge length of 1.0 mm. Figure 4 presents the assembly of the simulation, constituted of tool, sheet, backing plate and blank-holder. In order to reduce the simulation's total time, the initial hyperboloid diameter was decreased from 95 mm to 65 mm, and all other dimensions were kept the same to the ones used in the experiments.

The friction coefficient selected was of 0.1 (Coulomb Law) and the materials used were considered isotropic in the simulation. The tool's trajectory was configured by tabular motion and the temperature of the tool and the sheet were kept at 20 °C.

3 Results And Discussion

3.1 Experimental Results

We have listed in Table 3 the maximum axial force values for each SPIF experiment according to material, tool radius and initial thickness. Maximum axial force was obtained for the highest peak point in the force versus time graph for each experiment. The C and n parameters listed in Table 3 refer to the Ludwik–Hollomon equation.

In Fig. 5a we present a graph for axial force versus time considering SAE1008 steel with $s_0 = 0.75$ mm and using different tool radii ($R_t = 7.5, 5$ and 3 mm). In this figure, we were able to verify the force peak points in places where the tool moved on the z axis, followed by a lower force level due to circular trajectories.

For the experiment with $R_t = 7.5$ mm, we have indicated the point of maximum axial force ($F_{z_{max}}$), considering that after that point the force gradually reduces until an abrupt reduction in force occurs (also indicated in the Fig. 5a). The abrupt reduction point in axial force indicates that a crack was initiated during the experiment. Figure 5a indicates that the bigger the tool radius the greater the axial force required by the machine. This tendency is in accordance with other studies [4, 14, 25, 29] and can be explained as a consequence of contact area [13, 25].

Figure 5b presents a comparison between the axial force graphs for different initial thicknesses ($s_0 = 0.90, 0.75$ and 0.60 mm) for SAE1008 steel, using an $R_t = 5$ mm tool radius. In this Figure, we can see that the bigger that sheet's thickness, the greater the axial force required by the machine to perform the conformation process, as was reported in other studies [4, 14, 19, 25]. This tendency is related to the fact that with an increase in thickness, more material will have to be deformed by the tool, requiring more force [30].

In Fig. 5c we present a comparison of the axial force required according to material: C268 with $s_0 = 0.81$ mm, SAE1008 with $s_0 = 0.75$ mm and AA1200-H14 with $s_0 = 0.80$ mm, in which all experiments used tool radius $R_t = 5$ mm. It is possible to note in this Figure that the materials with greater tensile strength (Table 2) require greater force to be deformed, as was verified in the studies by Aerens et al. [14].

The force graphs presented in Fig. 5 present similar tendency to the one presented in other studies using the hyperboloid shape [23, 31, 32], and as such it is possible to observe that the axial force increases until it reaches a peak point, followed by a decrease in axial force intensity until a crack occurs in the sheet.

3.2 FEM Results

The axial force versus time graphs obtained in the FEM simulations were compared to the experimental graphs. The percentage errors in the maximum axial force estimates varied between 4.6 and 9.5%, as indicated in Table 4. This low percentage error margin allows us to conclude that the force data obtained in the FEM simulation were in agreement with the data seen in the experiments.

Table 4
FEM results

Exp.	Experimental outputs	FEM model predicted outputs	Percentage error (%)
	$F_{z_{max}}$ (N)	$F_{z_{max}}$ (N)	
7	2110.8	1995.2	9.5
14	2668.5	2790.0	4.6
25	638.9	699.6	5.5

Figure 6 indicates the experimental graph and the FEM simulation for the 25th experiment. This Figure also indicates the point where the beginning of the crack appears (experimental graph), and shows the maximum force point in the previous step-down, which was used as a comparison measure between the two graphs. In Fig. 6 it is also possible to identify the same tendency for force elevation in both graphs, even if the peak points are better described by the simulation than the mean force points (inferior level).

As indicated in Fig. 6, the force is overestimated by the model of finite elements when compared to the data found in the experiments, mainly at the beginning of the graph. This difference was also verified in the studies by Neto et al. [21], which attributed this fact to a possible slide between the sheet and the blank-holder, something that was not considered in the simulation.

3.3 Prediction of Force by Multiple Regressions

After constructing a multiple linear regression model, we were able to obtain Eq. 2, which related maximum axial force according to tool radius, initial sheet thickness, yield constant, material strain-hardening exponent and the interaction between these parameters. The R^2 obtained in these multiple regressions was of 98.85% and the maximum percentage error obtained by Eq. 2 in the experiments was of 11.5%, as indicated between square brackets beside the equation.

$$F_{z_{max}} = 416.7 + 172.8R_t + 275s_0 + 0.1479C - 5555n + 225.5R_t s_0 + 0.8436R_t C + 5.189s_0 C - 2929R_t n - 6284s_0 n + 1.585R_t s_0 C - 3727R_t$$

As indicated in Eq. 2, the increase in tool radius, initial thickness and yield constant have resulted in an increase of maximum axial force. However, the strain-hardening exponent had an inverse effect, since with its increase there is a decrease in maximum force. The same effect can be observed in every interaction with the strain-hardening exponent, which presents negative sign constants.

Unlike Aerens et al. [14]'s model, who used tensile strength in the force equation, in this work we have used the yield constant and the strain-hardening exponents in Ludwik–Hollomon's equation, because they allowed for the creation of a regression equation that better described the experimental results. Furthermore, Eq. 2 has also not taken into consideration the step-down, since, according to Duflou et al. [19], that is the parameter that least influences the force.

From the multiple quadratic regressions, we were able to elaborate maximum axial force equations for every material (Equations 3 to 5), in order to obtain estimated values with lower percentage error. The R^2 value for AA1200-H14 was of 99.75%, for SAE1008 was of 99.43% and for C268 was of 98.9%. The maximum percentage error in each regression equation per material varied between 3.7% and 10.9%, and is indicated beside each equation between square brackets.

$$Fz_{AA1200-H14} = 231.3 + 32.84R_t - 622.8s_0 + 110.6R_t s_0 - 2.206R_t^2 + 676.3s_0^2 [PE_{max} = 3.7\%] \quad (3)$$

$$Fz_{SAE1008} = -491.4 - 251.4R_t + 3574.8s_0 + 401.7R_t s_0 + 29.62R_t^2 - 961.9s_0^2 [PE_{max} = 4.3\%] \quad (4)$$

$$Fz_{C268} = 1940.8 - 652.4R_t - 1223.8s_0 + 413.5R_t s_0 + 64.04R_t^2 + 2362.9s_0^2 [PE_{max} = 10.9\%] \quad (5)$$

Figure 7 indicates response surface graphs for each multiple quadratic regression according to the materials. In these graphs it is possible to observe that Fz_{max} maximum axial force's tendency to increase varies according to Equations 3 to 5, and this variation occurs differently for each material since they present different mechanical properties.

4 Conclusions

In this study, we evaluated the influence of the tool radius, the initial thickness and the sheets' material properties (C and n) on the maximum axial force required for the SPIF process. After concluding the experiments, FEM simulations and multiple regressions, it is possible to conclude that:

1. The increase in tool radius, initial sheet thickness and yield constant, as well as reduction in the strain-hardening exponent, results in an increase of maximum axial force required for the SPIF process;
2. The FEM simulation presented good accuracy in predicting maximum axial force, validating the experimental values with a maximum percentage error of 9.5%;
3. Maximum axial force could be estimated by multiple linear regression equation according to C, n, s_0 and R_t , with a maximum error of 11.5%;
4. The elaboration of multiple quadratic regression equations for each material has allowed a reduction in percentage error to predict maximum axial force, with PE_{max} of 3.7% for aluminum, 4.3% for steel and 10.9% for brass.

Declarations

Funding: Not applicable.

Conflicts of interest/Competing interests: The authors declare no conflicts of interest.

Availability of data and material: Not applicable.

Code availability: Not applicable.

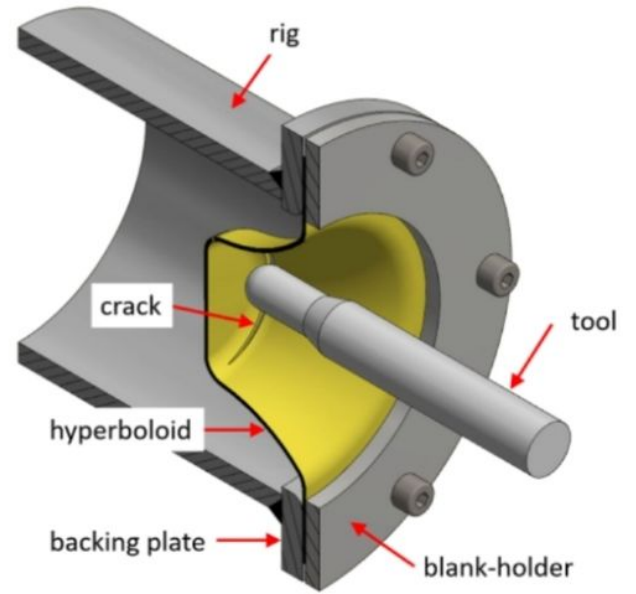
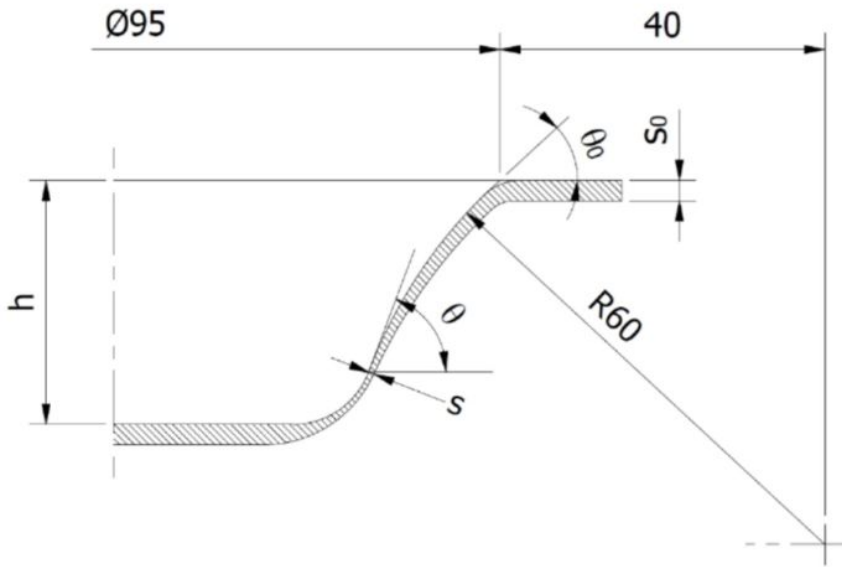
Authors' contributions: Not applicable.

References

1. Kumar SP, Elangovan S, Mohanraj R, Boopathi S (2021) A comprehensive review in incremental forming on approaches of deformation analysis and surface morphologies. *Mater Today Proc* 43:3129–3139. <https://doi.org/10.1016/j.matpr.2021.01.599>
2. More KR, Sisodia V, Kumar S (2021) A Brief Review on Formability, Wall Thickness Distribution and Surface Roughness of Formed Part in Incremental Sheet Forming. *Adv Manuf Process* 135–149. https://doi.org/https://doi.org/10.1007/978-981-15-9117-4_11 135
3. Scheffler S, Pierer A, Scholz P et al (2019) Incremental sheet metal forming on the example of car exterior skin parts. *Procedia Manuf* 29:105–111. <https://doi.org/10.1016/j.promfg.2019.02.112>
4. Chang Z, Li M, Chen J (2019) Analytical modeling and experimental validation of the forming force in several typical incremental sheet forming processes. *Int J Mach Tools Manuf* 140:62–76. <https://doi.org/10.1016/j.ijmachtools.2019.03.003>
5. Dabwan A, Ragab AE, Saleh MA et al (2020) Study of the Effect of Process Parameters on Surface Profile Accuracy in Single-Point Incremental Sheet Forming of AA1050-H14 Aluminum Alloy. *Adv Mater Sci Eng* 2020. <https://doi.org/10.1155/2020/7265941>

6. Mohanty S, Regalla SP, Rao YVD (2021) Effect of inclination and rotation of the sheet on sheet thinning and formability in robot assisted incremental sheet metal forming. *Mater Today Proc* 46:1039–1049. <https://doi.org/10.1016/j.matpr.2021.01.228>
7. Ambrogio G, Filice L, Gagliardi F (2012) Improving industrial suitability of incremental sheet forming process. *Int J Adv Manuf Technol* 58:941–947
8. Ben Said L, Bouhamed A, Wali M et al (2021) SPIF Manufacture of a Dome Part Made of AA1060-H14 Aluminum Alloy Using CNC Lathe Machine: Numerical and Experimental Investigations. *Arab J Sci Eng* 46:12207–12220. <https://doi.org/10.1007/s13369-021-05919-7>
9. Ismail NA, Ismail MIS, Radzman MAM et al (2019) Parametric optimization of robot-based single point incremental forming using Taguchi method. *Int J Integr Eng* 11:217–224. <https://doi.org/10.30880/ijie.2019.11.01.023>
10. Prakash Singh R, Kumar Gupta S, Kumar Singh P, Kumar S (2021) Robot assisted incremental sheet forming of Al6061 under static pressure: Preliminary study of thickness distribution within the deformation region. *Mater Today Proc* 47:2737–2741. <https://doi.org/10.1016/j.matpr.2021.03.056>
11. Amino M, Mizoguchi M, Terauchi Y, Maki T (2014) Current status of “Dieless” Amino’s incremental forming. *Procedia Eng* 81:54–62. <https://doi.org/10.1016/j.proeng.2014.09.128>
12. Azevedo NG, Farias JS, Bastos RP et al (2015) Lubrication aspects during Single Point Incremental Forming for steel and aluminum materials. *Int J Precis Eng Manuf* 16:589–595
13. Centeno G, Bagudanch I, Martínez-Donaire AJ et al (2014) Critical analysis of necking and fracture limit strains and forming forces in single-point incremental forming. *Mater Des* 63:20–29. <https://doi.org/10.1016/j.matdes.2014.05.066>
14. Aerens R, Eyckens P, Van Bael A, Duflou JR (2010) Force prediction for single point incremental forming deduced from experimental and FEM observations. *Int J Adv Manuf Technol* 46:969–982. <https://doi.org/10.1007/s00170-009-2160-2>
15. Jeswiet J, Micari F, Hirt G et al (2005) Asymmetric Single Point Incremental Forming of Sheet Metal. *CIRP Ann - Manuf Technol* 54:88–114. [https://doi.org/10.1016/S0007-8506\(07\)60021-3](https://doi.org/10.1016/S0007-8506(07)60021-3)
16. Torsakul S, Kuptasthien N (2019) Effects of three parameters on forming force of the single point incremental forming process. *J Mech Sci Technol* 33:2817–2823. <https://doi.org/10.1007/s12206-019-0528-2>
17. Al-Obaidi A, Kräusel V, Landgrebe D (2016) Hot single-point incremental forming assisted by induction heating. *Int J Adv Manuf Technol* 82:1163–1171. <https://doi.org/10.1007/s00170-015-7439-x>
18. Pereira Bastos RN, Alves de Sousa RJ, Fernandes Ferreira JA (2016) Enhancing time efficiency on single point incremental forming processes. *Int J Mater Form* 9:653–662. <https://doi.org/10.1007/s12289-015-1251-x>
19. Duflou J, Tunçkol Y, Szekeres A, Vanherck P (2007) Experimental study on force measurements for single point incremental forming. *J Mater Process Technol* 189:65–72. <https://doi.org/10.1016/j.jmatprotec.2007.01.005>
20. Li Y, Daniel WJT, Meehan PA (2017) Deformation analysis in single-point incremental forming through finite element simulation. *Int J Adv Manuf Technol* 88:255–267. <https://doi.org/10.1007/s00170-016-8727-9>
21. Neto DM, Martins JMP, Oliveira MC et al (2016) Evaluation of strain and stress states in the single point incremental forming process. *Int J Adv Manuf Technol* 85:521–534. <https://doi.org/10.1007/s00170-015-7954-9>
22. Wang J, Nair M, Zhang Y (2016) An Efficient Force Prediction Strategy in Single Point Incremental Sheet Forming. *Procedia Manuf* 5:761–771. <https://doi.org/10.1016/j.promfg.2016.08.062>
23. Duflou JR, Tunçkol Y, Aerens R (2007) Force Analysis for Single Point Incremental Forming. *Key Eng Mater* 344:543–550. <https://doi.org/10.4028/www.scientific.net/kem.344.543>
24. Li Y, Le, Liu ZB, Lu HB et al (2014) Experimental study and efficient prediction on forming forces in incremental sheet forming. *Adv Mater Res* 939:313–321. <https://doi.org/10.4028/www.scientific.net/AMR.939.313>
25. Bansal A, Lingam R, Yadav SK, Venkata Reddy N (2017) Prediction of forming forces in single point incremental forming. *J Manuf Process* 28:486–493. <https://doi.org/10.1016/j.jmapro.2017.04.016>
26. Schreiber RG, Teixeira AR, Pereira RSF et al (2021) Prototyping of absorber plate for solar collector by ISF and FSW processes. *J Brazilian Soc Mech Sci Eng* 43:1–12. <https://doi.org/10.1007/s40430-021-03083-5>
27. Haag J, Ferranti GO (2017) Estampabilidade De Aços De Baixo Carbono. 54º Semin. Laminação e Conform 54:308–319. <https://doi.org/10.5151/1983-4764-30515>
28. Maximiliano G, Schaeffer L, Daleffe A et al (2016) Estampagem Incremental de Múltiplos Passes em Chapa de Latão C268. 36º SENAFOR /19ª Conferência Nac Conform Chapas / 6ª Conferência Int Conform Chapas /3º Congr do BrDDR
29. Petek A, Kuzman K, Kopač J (2009) Deformations and forces analysis of single point incremental sheet metal forming. *Arch Mater Sci Eng* 35:107–116
30. Kumar A, Gulati V, Kumar P, Singh H (2019) Forming force in incremental sheet forming: a comparative analysis of the state of the art. Springer, Berlin Heidelberg
31. Xu D, Wu W, Malhotra R et al (2013) Mechanism investigation for the influence of tool rotation and laser surface texturing (LST) on formability in single point incremental forming. *Int J Mach Tools Manuf* 73:37–46
32. Malhotra R, Xue L, Belytschko T, Cao J (2012) Mechanics of fracture in single point incremental forming. *J Mater Process Technol* 212:1573–1590. <https://doi.org/10.1016/j.jmatprotec.2012.02.021>

Figures

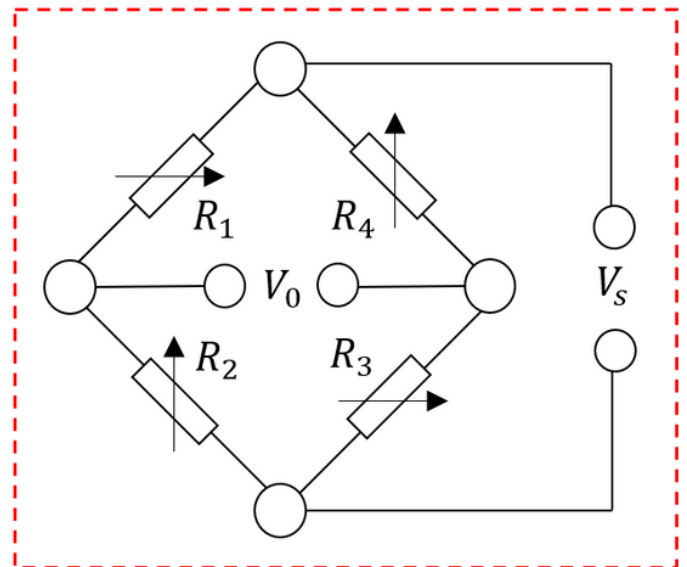
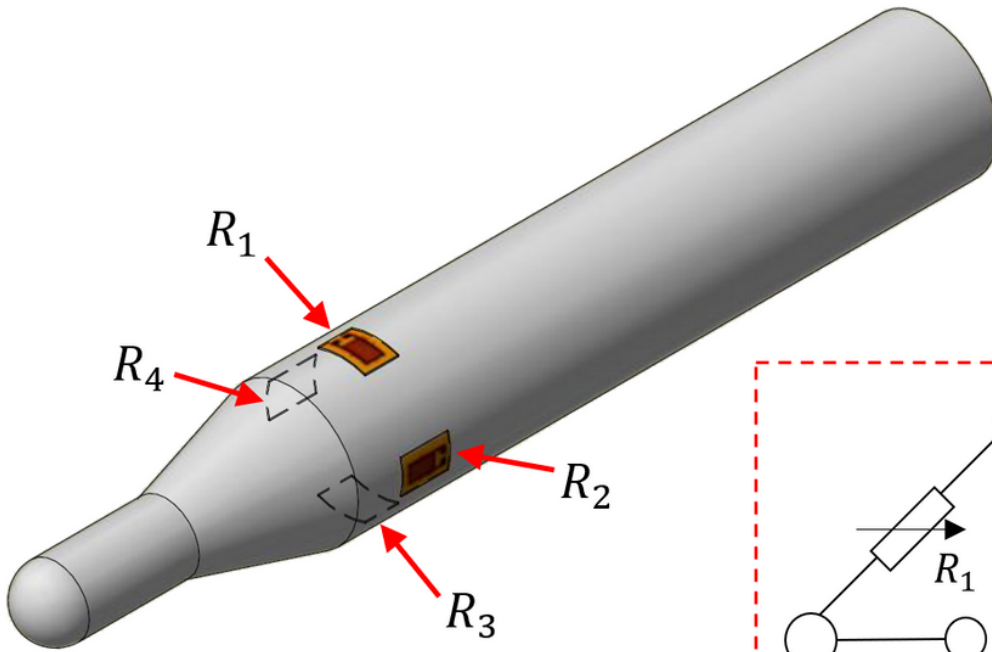


(a) (b)

Figure 1

a Hyperboloid shape used in the experiments

b Experiments' configuration



Wheatstone Bridge Circuit

Figure 2

Wheatstone bridge circuit in the tool

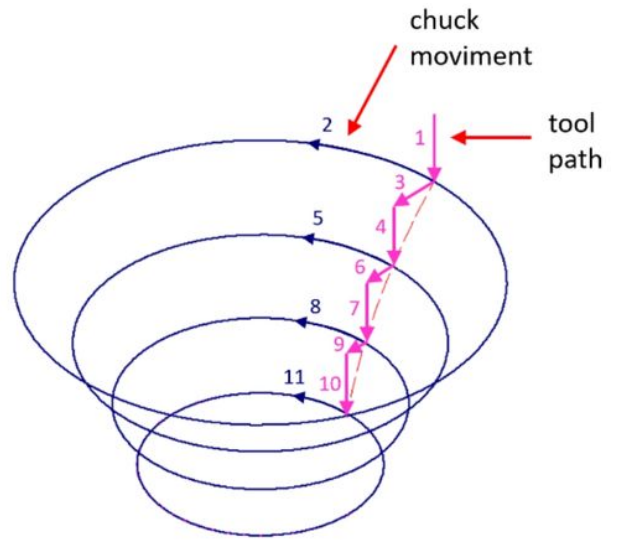
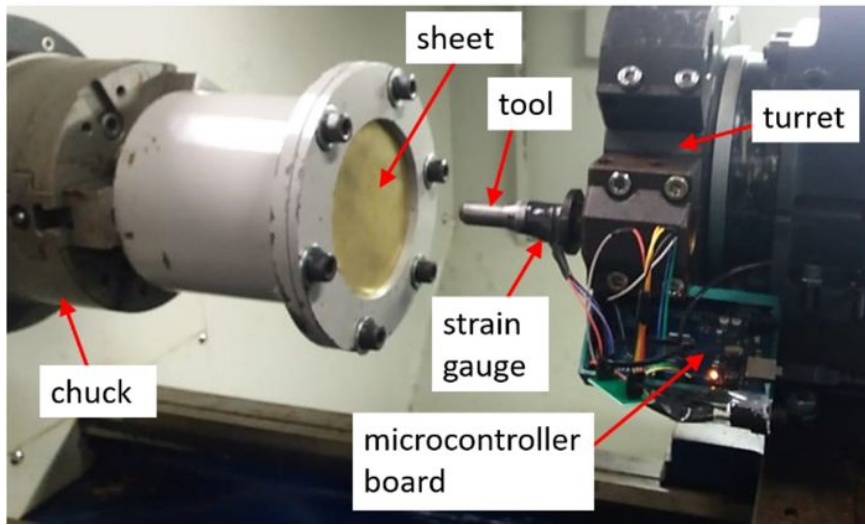


Figure 3

a Experiment configuration in a CNC lathe and b Tool trajectory in the experiments

Blank-holder

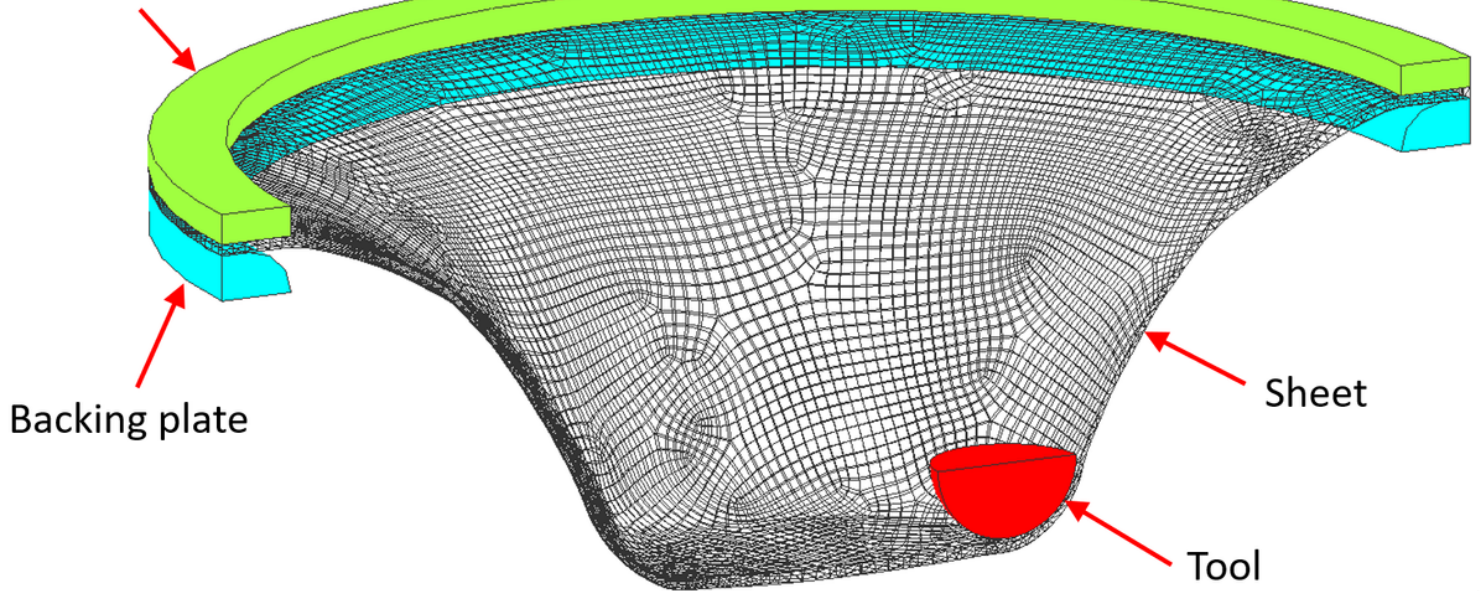


Figure 4

Assembly of SPIF test to FEM

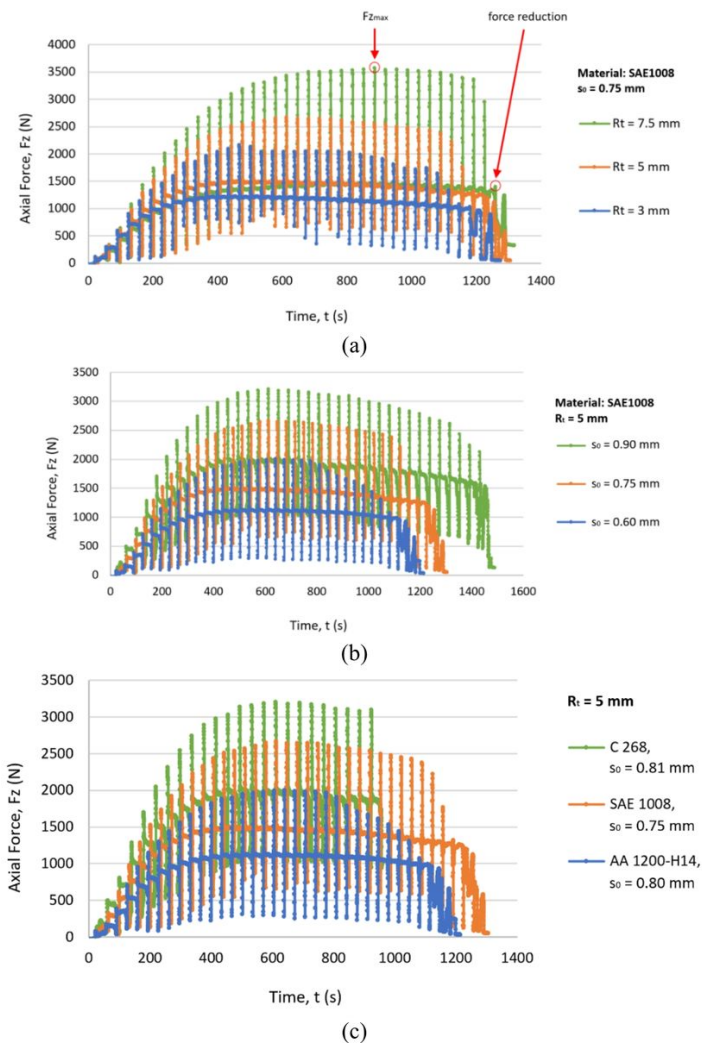


Figure 5
 Graph comparing forces: **a** Between different materials with $R_t = 5$ mm, **b** Between different tool radii for SAE1008 and $s_0 = 0.75$ mm and **c** Between different thicknesses for SAE1008 and $R_t = 5$ mm

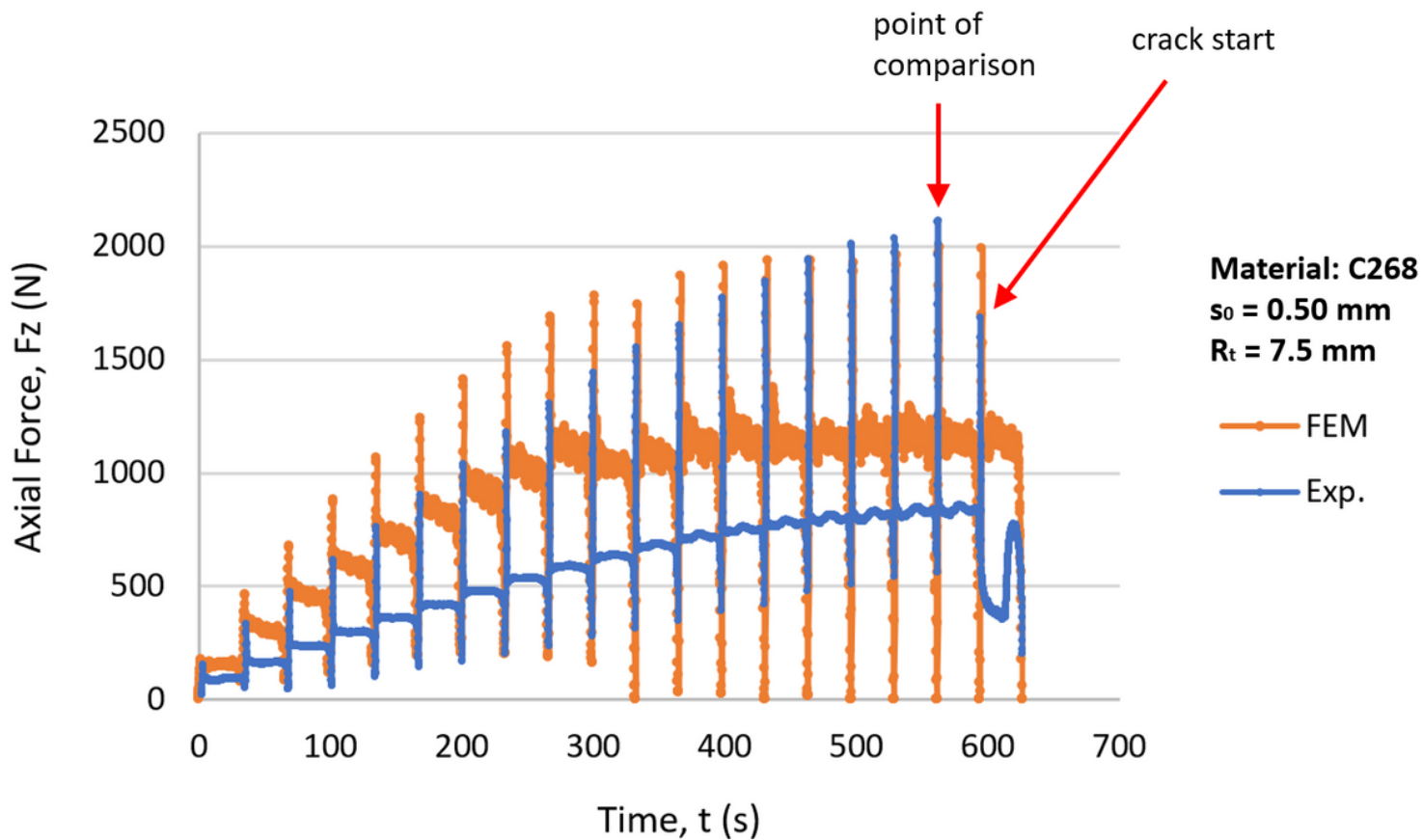
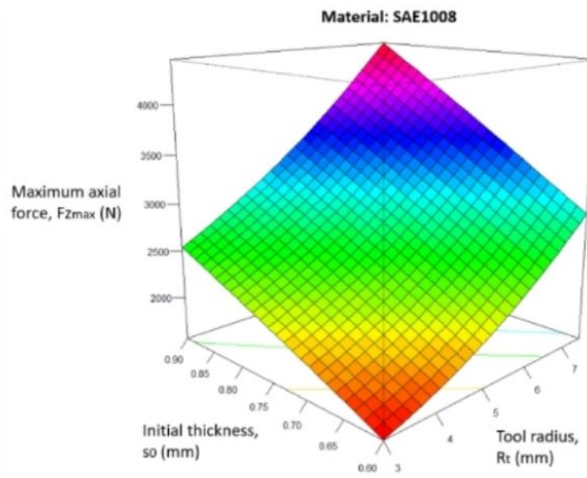
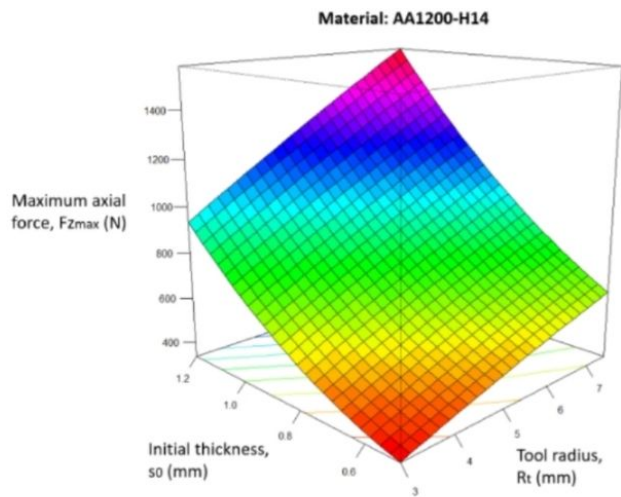
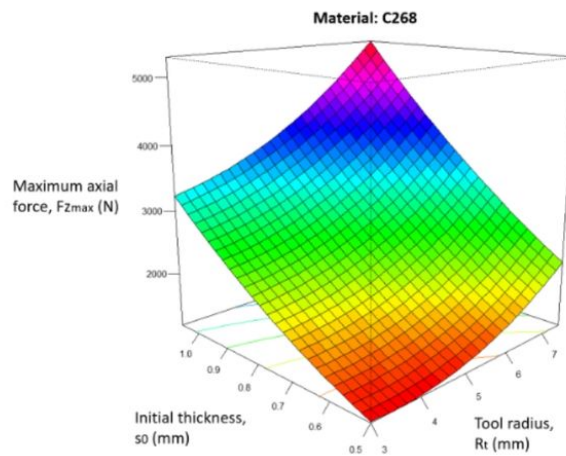


Figure 6

Graph comparing forces between experimental and FEM simulation values for C268 with $s_0 = 0.50 \text{ mm}$ and $R_t = 7.5 \text{ mm}$



(a) (b)



(c)

Figure 7

Graph for F_{zmax} response surface according to s_0 and R_t for

a AA1200-H14, **b** SAE1008 and **c** C268